Computational Analysis of Subsonic Vortex Interaction on Multi Swept Delta Wing Configurations

Michel Visonneau, Emmanuel Guilmineau, Jeroen Wackers

Computational Analysis of Subsonic Vortex Interaction on Multi Swept Delta Wing Configurations

Michel Visonneau*, Emmanuel Guilmineau†, Jeroen Wackers‡
CNRS - LHEEA, Centrale Nantes, France

This paper is part of the Special Session organized to report progress made by NATO AVT-316 on the topic Vortex Interaction Effects Relevant to Military Air Vehicle Performance. This collaborative research has been initiated to assess the capability of current CFD methods to predict vortex-interaction effects. In the present work, numerical simulations are performed with the ISIS-CFD flow solver by using a linear isotropic k-ω SST model and an hybrid RANS/LES DDES-SST turbulence closure for several angles of attack at symmetric (β = 0°) and moderate drift (β = 5°) conditions. For every turbulence closure, the anisotropic adaptive grid refinement functionality is used. A global and local flow assessment is conducted on the basis of experiments performed by TUM.

I. Introduction

Due to their excellent high angle of attack aerodynamic performance, delta or double-delta wings have been implemented in several advanced fighters. The flow over such wings is dominated by a pair of primary vortices that play a significant role in generating an additional lift at high angles of attack compared with a low-sweep-angle wing [1]. High angle of attack for aircraft is frequently encountered during landing and take-off phases, and during combat manoeuvring. The separated flow field is characterized by unsteady and strong vortical flow structures that can interact with various components of the aircraft and among themselves. These complicated flow interactions are the primary cause of most flight dynamic instabilities. Recently, an example of the flow simulation of the interaction between the inner and outer vortices of F-16XL aircraft has been published [2].

A low-aspect-ratio multiple-swept wing fuselage configuration is currently studied in the NATO STO AVT-316 task group on "Vortex Interaction Effects Relevant to Military Air Vehicle Performance". This collaborative research has been initiated to assess the capability of current CFD (Computational Fluid Dynamics) methods to predict vortex-interaction effects and extend our understanding of vortex-interaction flow physics for these problems through numerical and physical experimentation.

In this paper, we conduct a numerical simulation of the flow past this wing-fuselage combination at Mach number 0.15 for several angles of attack and two side slip angles, by means of RANS simulations and hybrid RANS-LES simulations. A comparison will be made between the numerical results and experimental data.

II. Test case

Figure 1 illustrates the test configurations [3, 4]. The first one is a triple delta wing configuration, the so-called NA1_W1, see Figure 1a, with three different consecutive wing sections featuring a varying leading-edge sweep. The inboard and outboard wing sections exhibit a medium leading-edge sweep of $\varphi_1 = \varphi_3 = 52.5°$ and the mid-board wing section is highly swept at $\varphi_2 = 75.0°$. The second one is a double delta configuration, the so-called NA1_W2, see Figure 1b, with two different consecutive wing sections of varying leading-edge sweeps characterized by a high leading-edge sweep of $\varphi_2 = 75.0°$ in the inboard wing section and a medium leading-edge sweep of $\varphi_3 = 52.5°$ in the outboard wing section. Both configurations have the same total length of l_{tot} = 1.160 m and the same root chord of c_r = 0.802 m.

Experiments are conducted in the wind tunnel of Technical University of Munich (TUM) for a speed of V_∞ = 51.97 m/s, which leads to a Reynolds number, based on c_r, of 2.36×10^6 and a Mach number of 0.15. Two side slip angles, β, are investigated: 0° and 5°.

*CNRS Research Director
†CNRS Senior Research Associate
‡Centrale Nantes Research Engineer

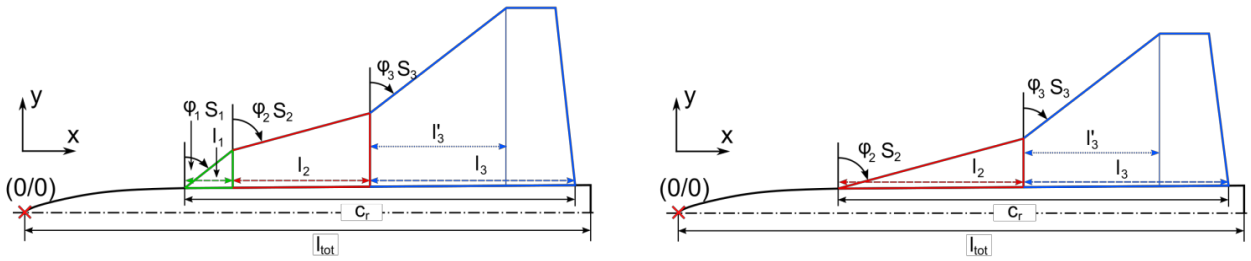

(a) Model NA1_W1 **(b) Model NA1_W2**

Fig. 1 Wing planforms

III. Flow Solver

The in-house solver ISIS-CFD developed by the authors, also available as a part of the FINE™/Marine computing suite worldwide distributed by Cadence Design Systems, is an incompressible multiphase unsteady Reynolds-averaged Navier-Stokes (URANS) solver mainly devoted to marine hydrodynamics. It is based on a fully-unstructured (face-based) finite volume discretization with specific functionalities needed for multiphase flows and industrial applications (see Queutey & Visonneau (2007) [5], Leroyer & Visonneau (2005) [6]). The method features several sophisticated turbulence models: apart from the classical two-equation k-ϵ and k-ω models, the anisotropic two-equation Explicit Algebraic Reynolds Stress Model (EARSM), as well as Reynolds Stress Transport Models, are available, see Deng et al. (1999) [7], Duvigneau & Visonneau (2003) [8] and [9]. All models are available with wall-function or low-Reynolds near wall formulations. Hybrid RANS/LES turbulence models based on Detached Eddy Simulation (DES-SST, DDES-SST, IDDES) are also implemented and have been thoroughly validated on automotive flows characterized by large separations, see Guilmineau et al. (2015) [10] and ships at steady drift [11]. Moreover, the solver accepts sliding and overset grids and features an anisotropic adaptive grid refinement functionality ([12], [13]) applied to unstructured hexahedral meshes which will be used extensively in this study.

IV. Anisotropic adaptive grid refinement

The grids employed in this study are generated with the help of the anisotropic adaptive grid functionality embedded in our flow solver ISIS-CFD, which is an essential element for complex-flow simulation due to the difficulty of creating high-resolution meshes for complex flows by hand. The choice of where to refine the grid is handled by the refinement criterion, formulated in the metric context [14, 15]. The criterion is a symmetric 3×3 tensor field computed from the flow, which indicates the desired local cell sizes in all directions. The actual mesh is then refined to fit this specification as closely as possible. The metric approach is very flexible; in this particular study, we use as refinement criteria, the so-called flux-component Hessian based on the second derivatives of the velocity fluxes and pressure. For all turbulence closures, computations are conducted in an unsteady way and the grid adaptation is based on averaged refinement criteria following the methodology described in [13]. For resolved turbulence, mesh refinement is no longer only a means to reduce the numerical error: the mesh resolution and the turbulence model influence each other and have to be mutually adjusted to obtain optimal results. For computations based on statistical (resp. hybrid RANS/LES) turbulence models, the grid is adapted every 10 (resp. 10) time steps in this specific study.

Figure 2 presents the converged flow-adapted grids used for the computations performed around the NA1_W1 with the k-ω SST and hybrid RANS/LES DDES-SST closures at an angle of attack of 24° for the symmetric and drift conditions. Only the cross-section x/c_r=0.592 is shown in this figure. For the symmetric (resp. drift) flow condition, the global flow-adapted grid for the k-ω SST simulation is comprised of 54.5M (resp. 89.6M) cells, 9.6 10^5 (resp. 17.1 10^5) faces on the wing surface, while the simulation realized with DDES-SST is comprised of 72.8M (resp. 97.9M) cells, 12.4 10^5 (resp. 28.4 10^5) faces on the wing surface. The typical size of cells inside the core of the main vortex is around 0.69mm to be compared with the local Taylor scale of 2.9 mm.

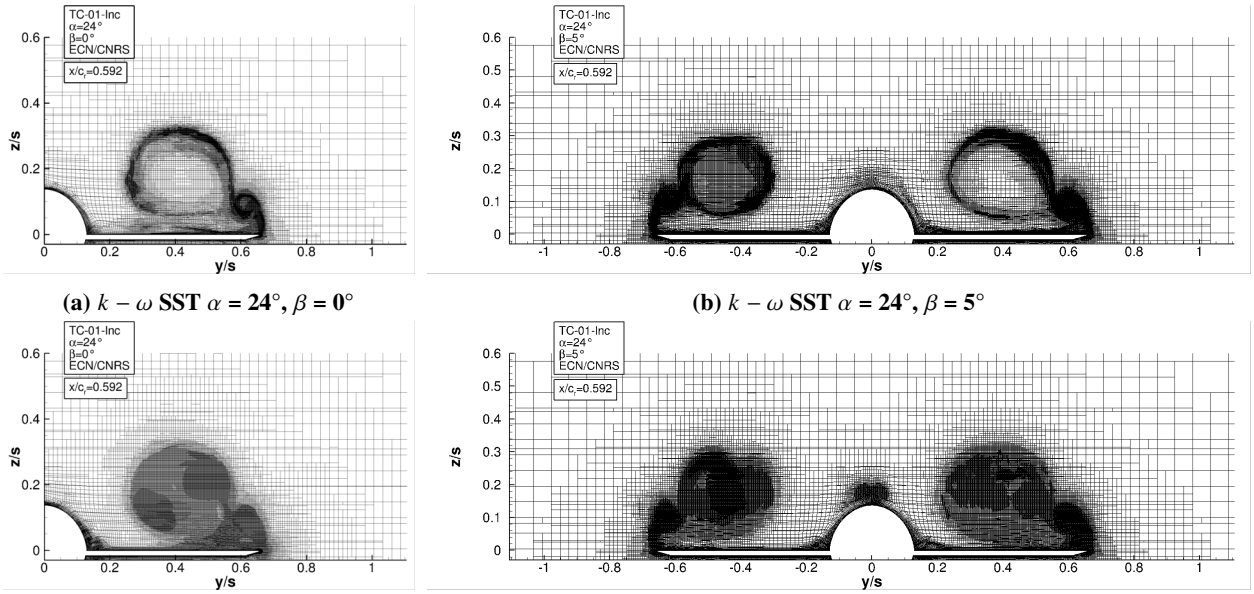

(a) $k-\omega$ **SST** α **= 24°,** β **= 0°**

(b) $k-\omega$ **SST** α **= 24°,** β **= 5°**

(c) DDES-SST α **= 24°,** β **= 0°**

(d) DDES-SST α **= 24°,** β **= 5°**

Fig. 2 NA1_W1 - Views of the flow-adapted grids at the cross-section x/c_r=0.592 with and without drift. Simulations performed with $k-\omega$ SST and DDES-SST.

V. Results

A. Symmetric Free-stream Conditions, β = 0°

1. Forces and moment

Figure 3 shows the evolution of the drag coefficient, C_D, the lift coefficient, C_L, and the pitching moment coefficient, C_{my}, versus the angle of attack, α, for the NA1_W1 and NA1_W2 configurations at β = 0°. For the configuration NA1_W1, see Figure 3a, the numerical results are in very good agreement with the experimental data, except for α = 32°. It is a bit disappointing to see that the hybrid RANS/LES DDES-SST closure does not bring any significant improvement at this high angle of attack. The shape variation of the pitching moment curve around the angle of attack 12°, due to the onset of vortex breakdown at the trailing edge, is well predicted with the k-ω SST model, which is very satisfactory. For the configuration NA1_W2, see Figure 3b, the vortex breakdown, observed at α = 23° in the experiments, leads to a local reduction of the lift coefficient. This local reduction of the lift is also predicted by the numerical simulations but at a smaller angle, α = 19° with the k-ω SST 1994 version (not shown here) and α = 20° with the k-ω SST 2003 version. The same behaviour is observed on the pitch moment C_{my} whose abrupt increase occurring in the experiments at α = 23°, is predicted too early at α = 20°. For higher angles of attack, the lift predicted by $k-\omega$ SST continues to grow without being able to represent the plateau observed in the experiments from α = 28°. Although the hybrid RANS-LES closure does not provide significantly better simulation in this range of moderate angles of attack, i.e. for α comprised between 20° and 24°, it is reassuring to see that its prediction of drag, lift and pitch moment at a high angle of attack α = 32°, is now in perfect agreement with TUM measurements.

2. Angle of attack α=16°

Figure 4 presents the vortical structures obtained with both turbulence models for the angle of attack α = 16° and both wing configurations. These figures show the isosurface of the dimensionless second invariant, Q^* = 50, the blue translucent surface, and the zero-isosurface of the Cartesian axial component of the velocity, the red surface, which indicates a reverse flow. For NA1_W1, the flow is characterized by two primary leading-edge vortices. The first vortex develops at the most inboard wing section and is called inboard vortex (IBV). The second vortex develops at the kink from the highly swept to the medium swept wing section at x/c_r = 0.475 and is called mid-board vortex (MBV). All

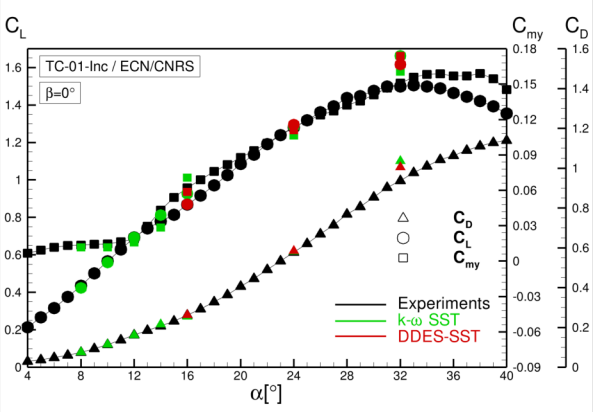

(a) Model NA1_W1

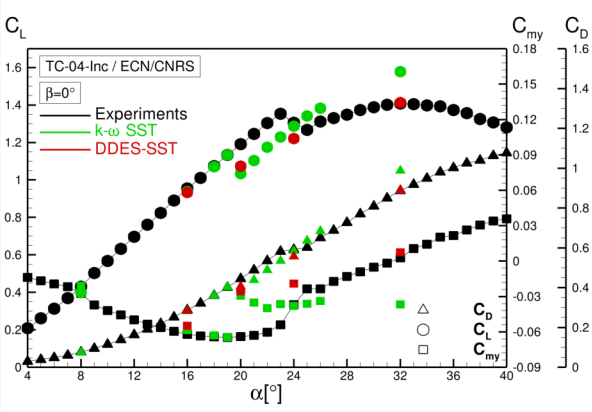

(b) Model NA1_W2

Fig. 3 Longitudinal aerodynamic coefficients for the NA1_W1 and NA1_W2 configurations versus the angle of attack α and $\beta = 0°$.

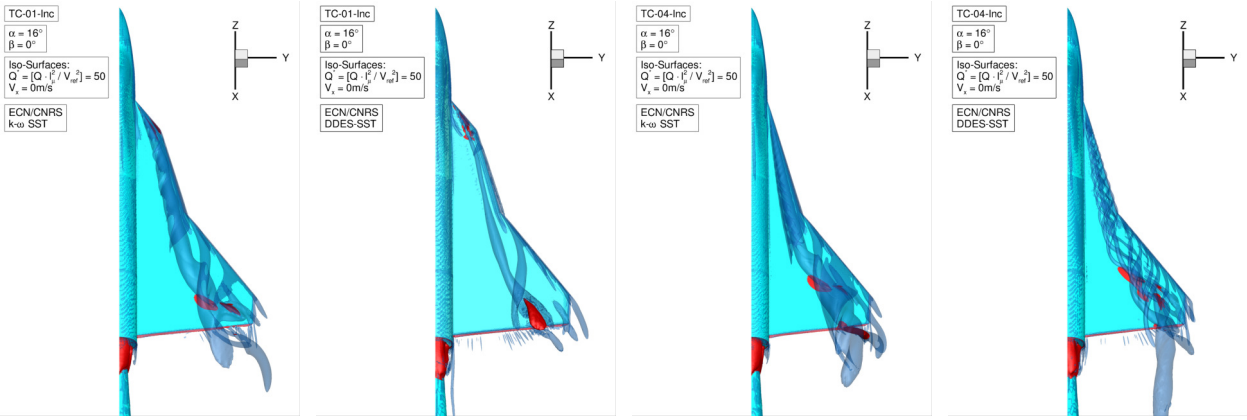

(a) NA1_W1 - k-ω SST (b) NA1_W1 - DDES-SST (c) NA1_W2 - k-ω SST (d) NA1_W2 - DDES-SST

Fig. 4 Vortical structures of the NA1_W1 and NA1_W2 configurations for $\alpha = 16°$ and $\beta = 0°$.

these structures are predicted by every turbulence model. However, the size of these structures is thinner with the DDES-SST model, indicating more intense vortices. For the second wing configuration NA1_W2, k-ω SST predicts a similar unique IBV vortex while DDES-SST simulation provides a collection of peripheral vortices spiraling around a thinner vortex. The interaction with the second vortex MBV, originating from the medium swept wing, leads to a local zone of reverse flow as indicated by the red region which occurs more upstream than in the NA1_W1 configuration for both turbulence models. However, for DDES-SST, the detached layer simulated by k-ω SST is replaced by a collection of individual thinner longitudinal vortices originating from the leading edge of the medium swept wing (Fig. 4d).

Fig. 5 shows the surface pressure distribution and skin friction lines for both wings and turbulence closures. NA1_W1 has a lower surface pressure zone on the medium swept wing for $k - \omega$ SST which is not present in the DDES-SST simulation, indicating a more intense and stable longitudinal vortex, as expected from a DDES-SST turbulence closure. For NA1_W2, no major differences between the two simulations are visible in the surface pressure distribution and skin friction lines.

Figure 6 shows the dimensionless axial velocity component at the cross-section x/c_r=0.592 for both wing profiles at an angle of attack $\alpha = 16°$. Results obtained with k-ω SST and DDES-SST turbulence closures are compared with TUM experiments. First of all, the IBV vortex in the experiments has a wake-type for NA1_W1 and jet-type for NA1_W2. For NA1_W1, this characteristic is not captured by k-ω SST which does not simulate the strong decrease of the longitudinal velocity, while DDES-SST provides a very accurate solution which captures this characteristic evolution in the core of the main vortex. The MBV vortex is also more intense with DDES-SST and in better agreement with TUM experiments.

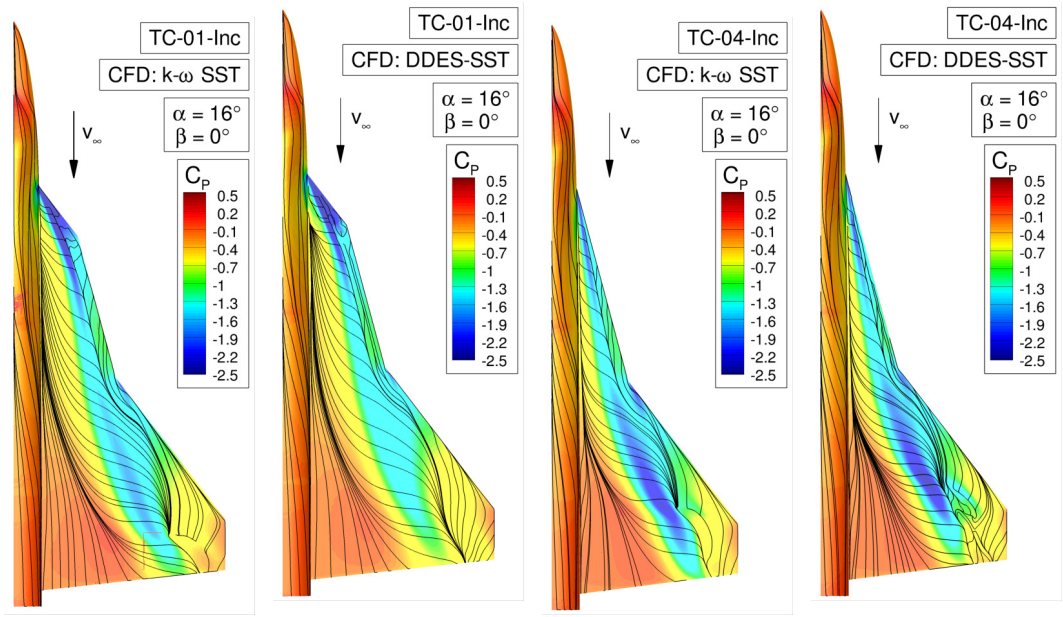

(a) NA1_W1 - k-ω SST (b) NA1_W1 - DDES-SST (c) NA1_W2 - k-ω SST (d) NA1_W2 - DDES-SST

Fig. 5 Surface pressure distribution and skin friction lines on the NA1_W1 and NA1_W2 configurations for α = 16° and β = 0°.

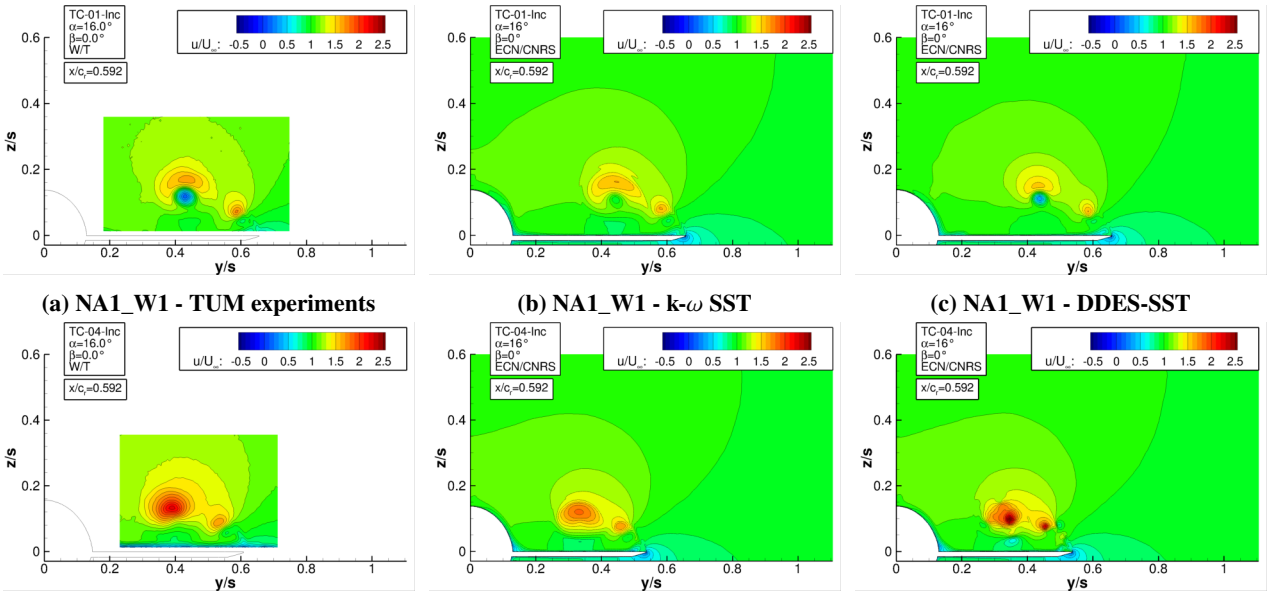

(a) NA1_W1 - TUM experiments (b) NA1_W1 - k-ω SST (c) NA1_W1 - DDES-SST

(d) NA1_W2 - TUM experiments (e) NA1_W2 - k-ω SST (f) NA1_W2 - DDES-SST

Fig. 6 Axial component of the velocity at x/c_r = 0.592 for the NA1_W1 and NA1_W2 configurations at α = 16° and β = 0°.

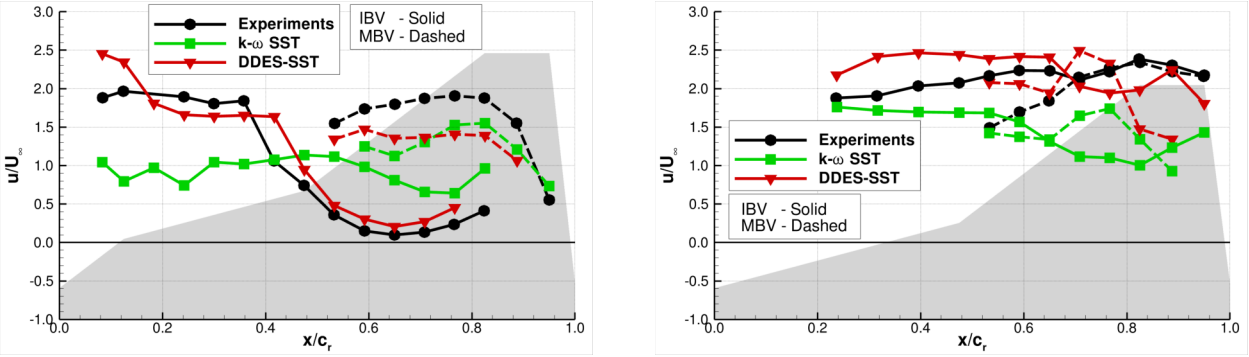

(a) Model NA1_W1 **(b) Model NA1_W2**

Fig. 7 Dimensionless axial velocity for IBV and MBV of the NA1_W1 and NA1_W2 configurations for α = 16° and β = 0°.

DDES-SST performs also better for NA1_W2 since it gives a stronger axial velocity component than $k-\omega$ SST in the core of the IBV, again in good agreement with TUM experiments. However, the axial velocity component in the MBV vortex is overestimated by DDES-SST.

For both wings, Figure 7 shows the dimensionless axial velocity, u/U_∞, extracted at the cores of the inboard (IBV) and mid-board (MBV) vortices for the angle of attack α = 16°. As mentioned previously, for NA1_W1, in the experiments, the vortex core in the IBV first shows a jet-type core flow with $u/U_\infty \simeq 2$. After $x/c_r \simeq 0.36$, the axial velocity decreases continuously until it reaches 0.1 at $x/c_r \simeq 0.65$. Then the velocity increases slowly as it approaches the trailing edge of the wing. This flow change from a jet-type core to a wake-type core flow is well predicted by the DDES-SST turbulence model. With the k-ω SST turbulence model, the high level of axial velocity at the onset of the vortex is not predicted. For the configuration NA1_W2, a jet-type core flow is observed for the IBV in the experiments for which an almost constant level of u/U_∞ is obtained with a slight tendency to increase. With the k-ω SST turbulence model, the axial velocity in the core of the IBV is in agreement with the experimental data at the onset of the vortex but the velocity decreases continuously until $x/c_r \simeq 0.82$, while DDES-SST is able to maintain a high level core flow plateau as shown in the TUM measurements.

3. Angle of attack α=24°

Figure 8 presents the vortical structures obtained by the two turbulence models for the angle of attack α = 24° and both wing configurations. For NA1_W1, both IBV and MBV vortices are present with a reverse flow in the core of IBV

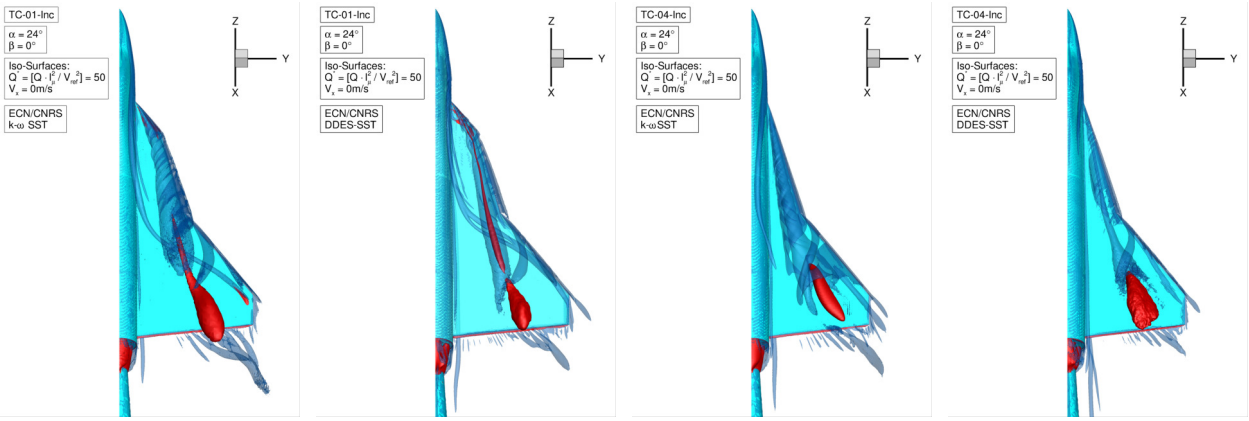

(a) NA1_W1 - k-ω SST **(b) NA1_W1 - DDES-SST** **(c) NA1_W2 - k-ω SST** **(d) NA1_W2 - DDES-SST**

Fig. 8 Vortical structures of the NA1_W1 and NA1_W2 configurations for α = 24° and β = 0°.

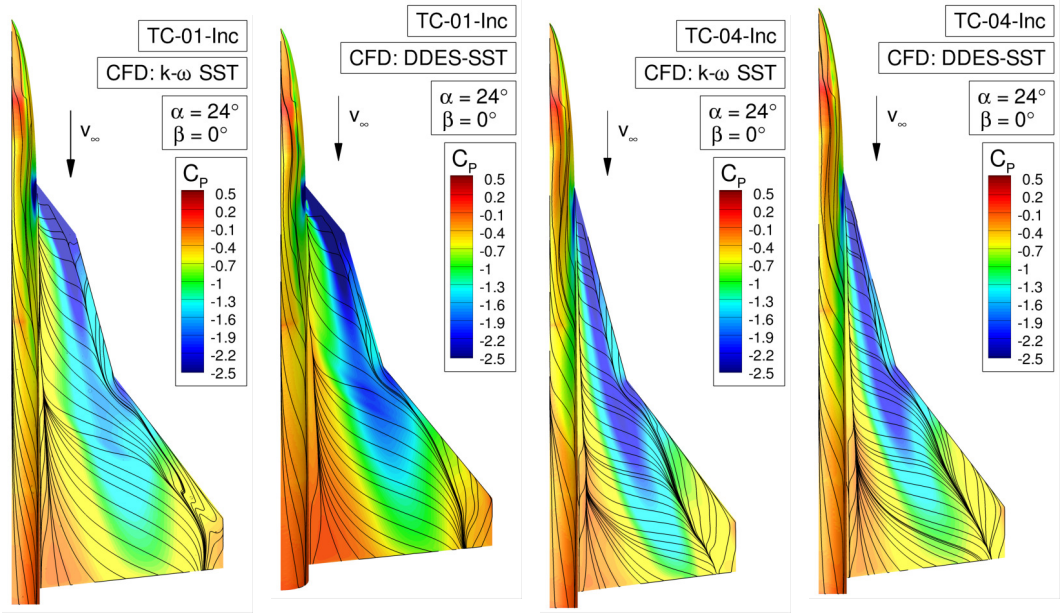

(a) NA1_W1 - k-ω SST (b) NA1_W1 - DDES-SST (c) NA1_W2 - k-ω SST (d) NA1_W2 - DDES-SST

Fig. 9 Surface pressure distribution and skin friction lines on NA1_W1 and NA1_W2 configurations for α = 24° and β = 0°.

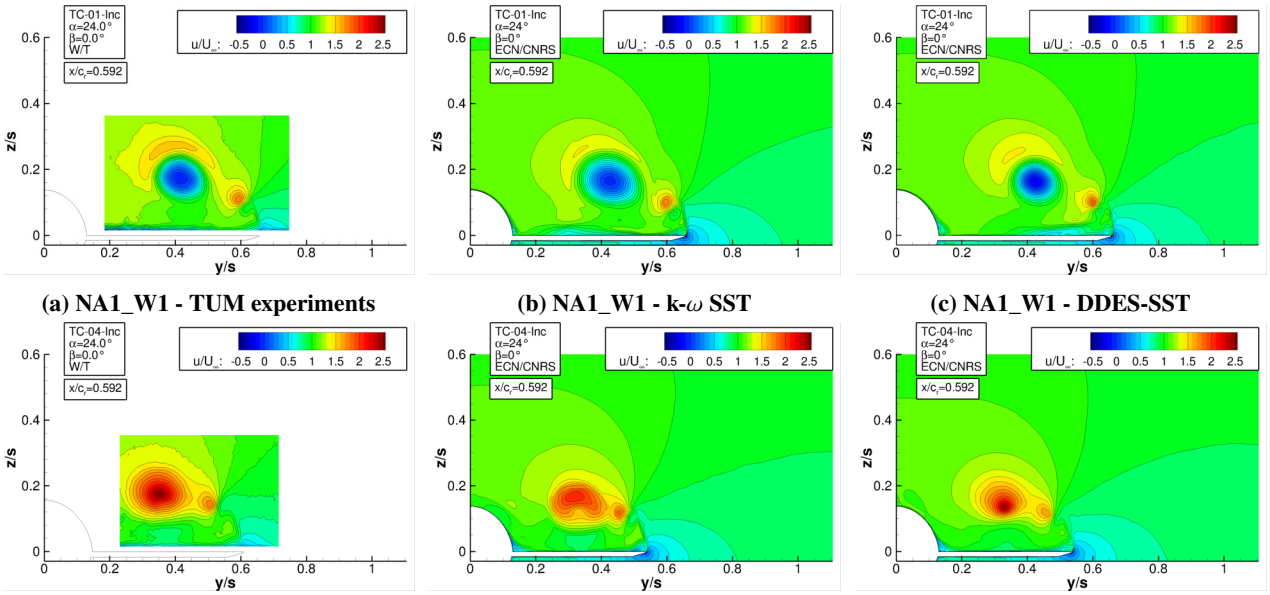

(a) NA1_W1 - TUM experiments (b) NA1_W1 - k-ω SST (c) NA1_W1 - DDES-SST

(d) NA1_W2 - TUM experiments (e) NA1_W2 - k-ω SST (f) NA1_W2 - DDES-SST

Fig. 10 Axial component of the velocity at x/c_r = 0.592 for the NA1_W1 and NA1_W2 configurations at α = 24° and β = 0°.

starting earlier than for the previous angle of attack. Both turbulence closures predict the existence of a third vortex parallel to the fuselage during the first part of its path and then deviated towards the outer part of the wing, leading to a potentially more complex vortex interaction than for the lower angle of attack. For NA1_W2, the two main vortices IBV and MBV are present with a reverse flow starting later. Moreover, the third vortex emanating close to the fuselage is also found for this wing but its path remains parallel to the fuselage.

Fig. 9 shows the surface pressure distribution and skin friction lines for both wings and turbulence closures at this angle of attack. For NA1_W1, the blue zone associated with the local reverse flow is larger for DDES-SST than with k-ω SST. For NA1_W2, this low pressure zone is less extended and, contrary to the previous wing, DDES-SST provides a slightly reduced low surface pressure region, compared to k-ω SST.

Figure 10 shows the axial velocity component at the cross-section x/c_r=0.592 for both wing profiles at an angle of attack α = 24°. For NA1_W1, as observed previously for α = 16°, the IBV vortex has a marked wake-type illustrated by the large region of very low axial velocity in its core at this cross-section. k-ω SST predicts qualitatively this trend but still over-estimates the axial velocity in the core of IBV. On the contrary, DDES-SST captures the right almost negative value of the axial velocity in the core and yields a more confined vortex in better agreement with TUM experiments. For NA1_W2, the IBV vortex has still a marked jet-type and DDES-SST is again the only model able to capture accurately the overshoot on the core axial velocity component, $k-\omega$ SST providing only a fair qualitative trend.

Figure 11 shows the dimensionless axial velocity, u/U_∞, in the inboard vortex (IBV) and the mid-board vortex (MBV) cores for the angle of attack α = 24°. For NA1_W1, both models under-predict the core velocity at the onset but DDES-SST is the only one able to capture the low velocity, close to zero, observed from the middle of the wing. For NA1_W2, the axial velocity is overestimated by DDES-SST at the onset of IBV but the rapid decay of the core velocity around x/c_r=0.6 is better captured by this hybrid RANS/LES model.

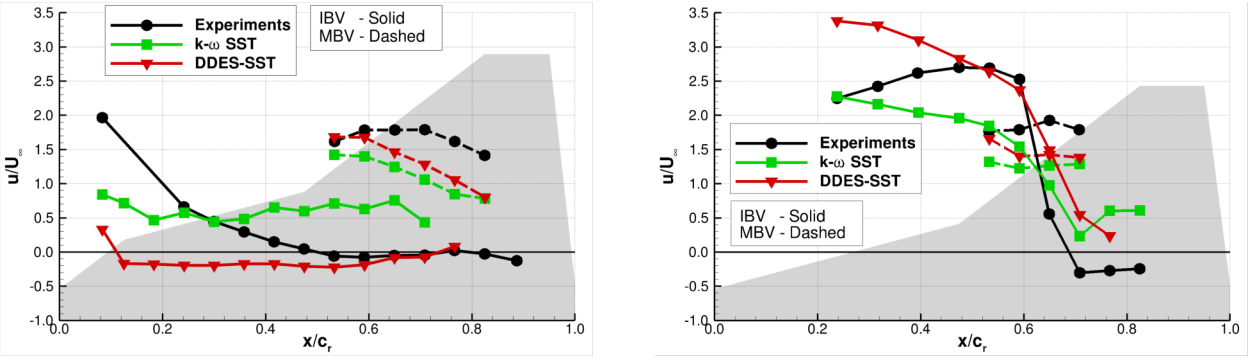

(a) Model NA1_W1 **(b) Model NA1_W2**

Fig. 11 Dimensionless axial velocity for IBV and MBV of the NA1_W1 and NA1_W2 configurations for α = 24° and β = 0°.

4. Angle of attack α=32°

Figure 12 presents the vortical structures obtained by the two turbulence models for the angle of attack α = 32° and both wing configurations. For both turbulence closures, the main IBV vortex exhibits a core fully contaminated with a reverse flow from its onset to its destabilisation for NA1_W1. Moreover, the MBV vortex seems to disappear quickly, at least as shown by the iso-Q* surface although we will see further from the cross-sectional views that it is still present. Two vortices emanate from the fuselage, instead of one for the previous angle of attack. These vortices are deviated towards the outer part of the wing at a location situated more upwind compared to the previous angle of attack but their interaction with the IBV is not visible in the cross-sectional views which will be shown next. For the NA1_W2 configuration, the global topology is very similar but the reverse flow in the core of IBV appears only at some distance from the onset, closer to the leading edge for DDES-SST than for k-ω SST.

Fig. 13 shows the surface pressure distribution and skin friction lines for both wings and turbulence closures. As expected, the blue low surface pressure region is more extended for NA1_W1 than for NA1_W2. Figure 14 shows the axial velocity component at the cross-section x/c_r=0.592. For this high angle of attack, TUM experiments reveal that both wing profiles have a wake-type IBV vortex and slightly different longitudinal velocity distribution in the MBV

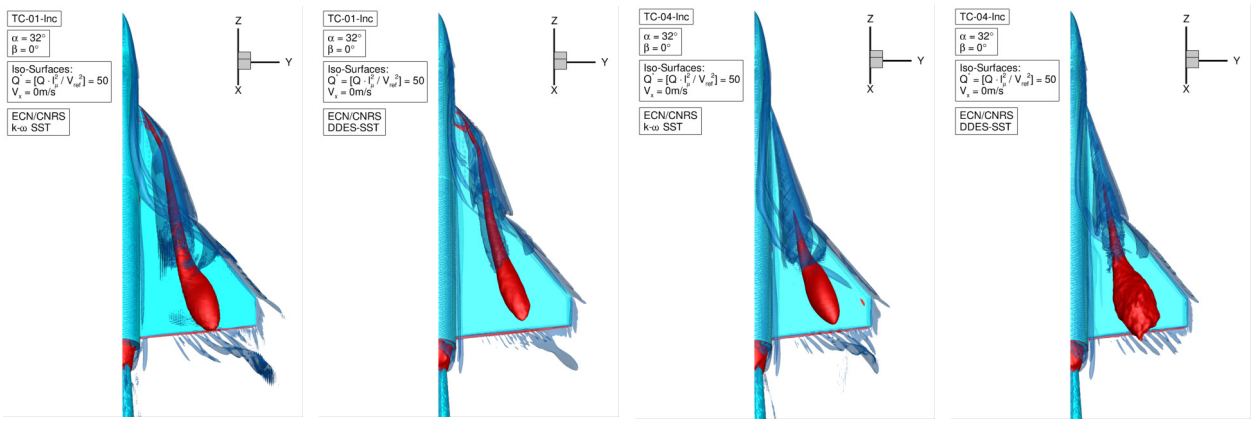

(a) NA1_W1 - k-ω SST **(b) NA1_W1 - DDES-SST** **(c) NA1_W2 - k-ω SST** **(d) NA1_W2 - DDES-SST**

Fig. 12 Vortical structures of the NA1_W1 and NA1_W2 configurations for α = 32° and β = 0°.

vortex core at this cross-section. For NA1_W1 and NA1_W2, the radius of the low-velocity IBV core is under-estimated by both turbulence closures at this location, DDES-SST being the model which provides the thinnest core. For NA1_W2, k-ω SST predicts a significantly higher axial velocity around the low-velocity core, a result which is not confirmed by the experiments. For the MBV vortex, $k-\omega$ SST predicts a jet type core while the prediction of DDES-SST, with a weaker longitudinal velocity appears to be in better agreement with TUM experiments.

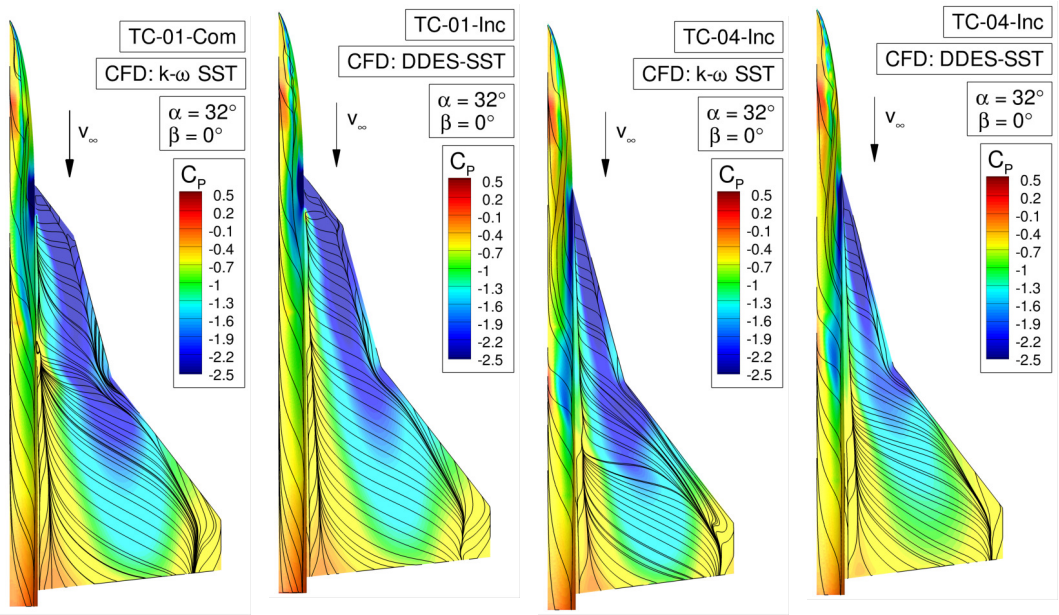

(a) NA1_W1 - k-ω SST **(b) NA1_W1 - DDES-SST** **(c) NA1_W2 - k-ω SST** **(d) NA1_W2 - DDES-SST**

Fig. 13 Surface pressure distribution and skin friction lines on NA1_W1 and NA1_W2 configurations for α = 32° and β = 0°.

Figure 15 shows the dimensionless axial velocity, u/U_∞, at the core of the inboard vortex (IBV) and the mid-board vortex (MBV) for the angle of attack α = 32°. For NA1_W1, both k-ω SST and DDES-SST are in very good agreement with TUM experiments since they predict the correct low and negative axial velocity plateau from the onset and during its progression to the trailing edge. For NA1_W2, the longitudinal evolution of the axial component of the velocity is characterised by a rapid decay occurring for x/c_r between 0.4 and 0.5. DDES-SST is able to capture the rapid decay,

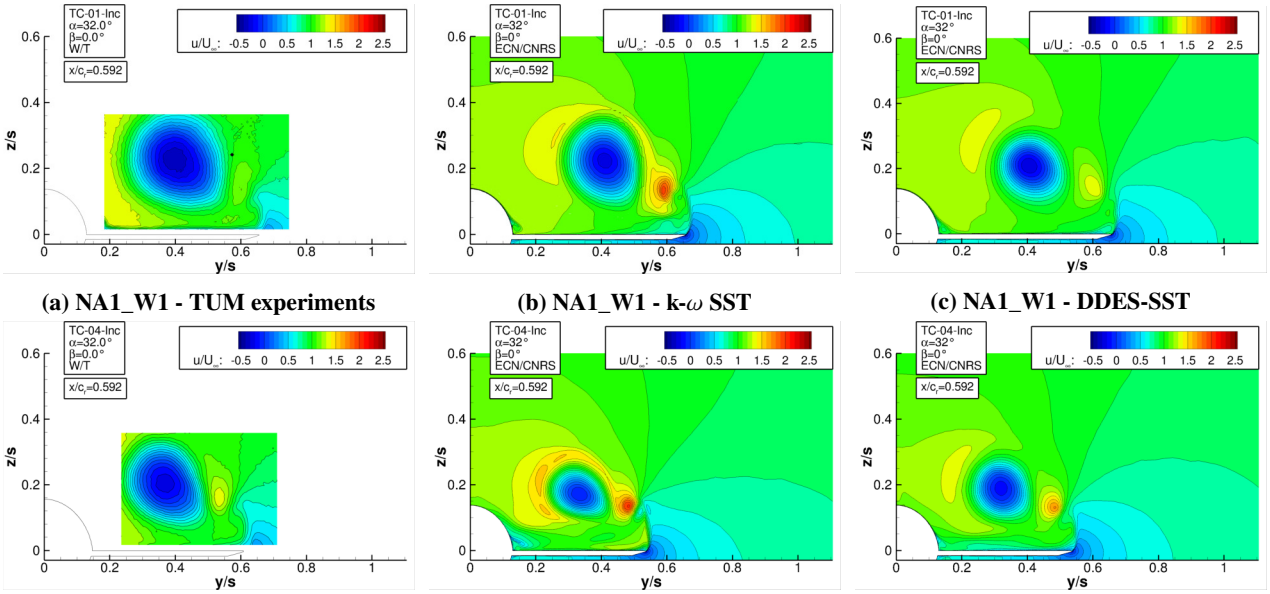

(a) NA1_W1 - TUM experiments **(b) NA1_W1 - k-ω SST** **(c) NA1_W1 - DDES-SST**

(d) NA1_W2 - TUM experiments **(e) NA1_W2 - k-ω SST** **(f) NA1_W2 - DDES-SST**

Fig. 14 Axial component of the velocity at $x/c_r = 0.592$ for the NA1_W1 and NA1_W2 configurations at $\alpha = 32°$ and $\beta = 0°$.

although slightly anticipated for x/c_r between 0.3 and 0.4. However, DDES-SST overpredicts by 200% the core axial velocity component from the onset region to the zone of sudden decay. On the other hand, k-ω SST provides a core axial velocity in good agreement with TUM experiments from the onset to x/c_r =0.3 and captures accurately the rapid decay which is observed in the experiments.

B. Side Slip Angle Conditions, $\beta = 5°$.

1. Forces and moments

Figure 16 presents the evolution of the forces and moments coefficients versus the angle of attack for the configuration NA1_W1. For the longitudinal aerodynamic coefficients, see Figure 16a, the shape of the curves is comparable to that

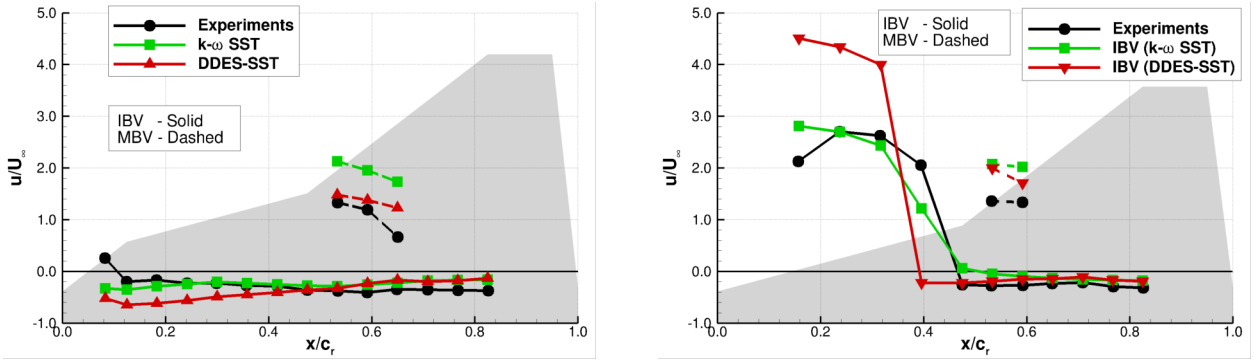

(a) Model NA1_W1 **(b) Model NA1_W2**

Fig. 15 Dimensionless axial velocity for IBV and MBV of the NA1_W1 and NA1_W2 configurations for $\alpha = 32°$ and $\beta = 0°$.

obtained for $\beta = 0°$ with however, some minor differences. The main difference is the shift of the angle where the vortex breakdown occurs. In the experiments, this phenomenon occurs at $\alpha \simeq 15°$ with drift instead of 12° without drift. For this configuration, the numerical results obtained with the k-ω SST and DDES-SST turbulence models are in good agreement with the experimental data for the drag and lift, the hybrid RANS/LES closure providing a slightly improved prediction of the pitch moment over the whole range of simulations. The agreement between measurement and simulation is less satisfactory for the lateral aerodynamic coefficients, see Figure 16b. On one hand, the side-slip coefficient C_s and C_{mz} coefficient are accurately predicted $k - \omega$ SST and DDES-SST, with a slight improvement brought by DDES-SST for the highest computed angle of attack, α=24°. On the other hand, the numerical prediction of the roll moment coefficient C_{mx} is inaccurate for $k - \omega$ SST which is not able to capture the decay and the change of slope occurring around 16°. Hybrid RANS/LES computations look more promising at α=16° with the right negative value and the sudden growth at $\alpha = 18°$ where the roll moment coefficient is close to zero, in good agreement with the measurements. But for the higher angles of attack, i.e. 20°and 24°, the roll moment coefficient decreases again instead of keeping close to zero, as indicated in the experiments. This change of trend between 16°, 18° and 20° needs to be correlated to the local behaviour of the leeward and windward vortices. Of course, the range of variation of the roll moment being very small, it is hard to simulate accurately and to track in the local flow characteristics.

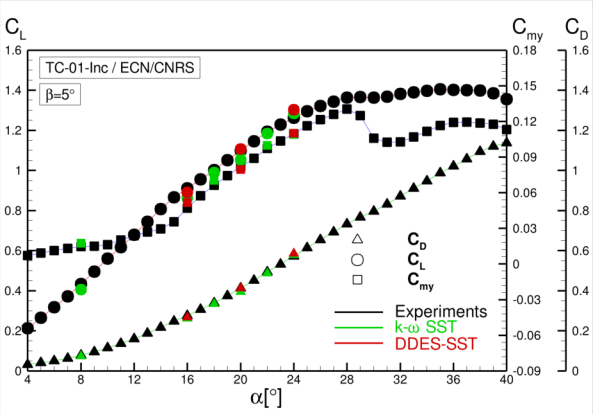

(a) Longitudinal coefficients

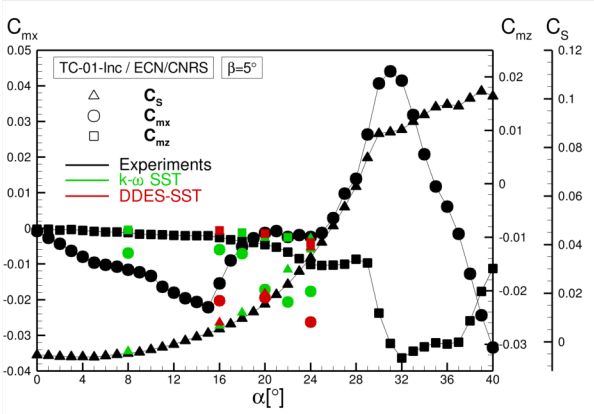

(b) Lateral coefficients

Fig. 16 Longitudinal and lateral aerodynamic coefficients for the NA1_W1 configuration for $\beta = 5°$ versus the angle of attack α.

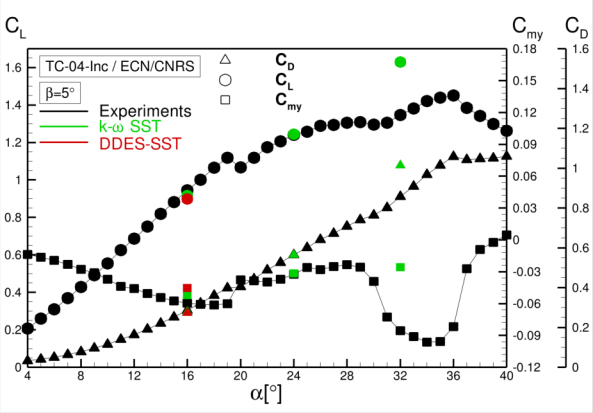

(a) Longitudinal coefficients

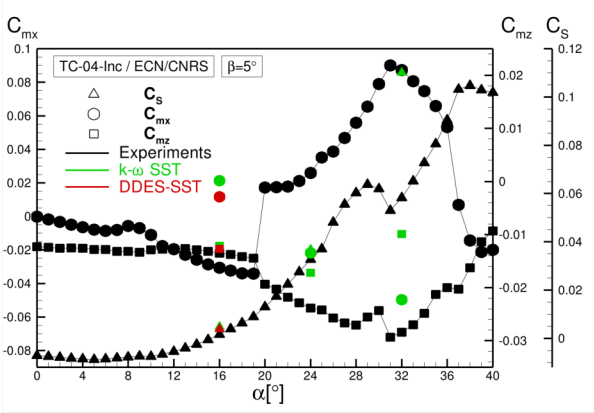

(b) Lateral coefficients

Fig. 17 Longitudinal and lateral aerodynamic coefficients for the NA1_W2 configuration for $\beta = 5°$ versus the angle of attack α.

Figure 17 presents the evolution of the forces and moments coefficients versus the angle of attack for the configuration

NA1_W2. For the longitudinal aerodynamic coefficients, see Figure 17a, only three angles of attack are computed with both k-ω SST and DDES-SST and the agreement is quite good on the three longitudinal force and moment coefficients for the first two angles of attack, i.e. 16°and 24°. At 32°, the k-ω model reaches its limits and provides too high values of drag, lift and pitch moment coefficients. As noticed for the NA_W1 wing profile, the situation is more complex for the lateral force and moment coefficients. At 16°, both turbulence models provide evaluations of C_S and C_{mz} in good agreement with TUM measurements. For higher angles of attack, k-ω SST is unable to capture the monotonous decay of C_{mz} up to 32°. Its prediction of C_S is still good at 24°, but strongly overestimates its growth at 32°. As noticed for the previous wing profile, the behaviour of the roll moment, with its change of sign around 20°, is more difficult to capture. Both k-ω SST and DDES-SST predict a positive roll moment coefficient at a lower angle of attack of 16° but for higher angles of attack, i.e 24° and 32°, the roll moment coefficient gets negative and decays, with values which are opposite to the experiments.

2. Angle of attack α=16°

Figs. 18 and 19 show the vortical structures, surface pressure distributions and skin friction lines for NA1_W1 and NA1_W2 at 16°. For both leeward and windward wings, the IBV vortex is thinner, more intense and more stable when computed with DDES-SST, leading to a local increase of the surface pressure under the trajectory of this vortex. Both wing configurations are concerned by this observation.

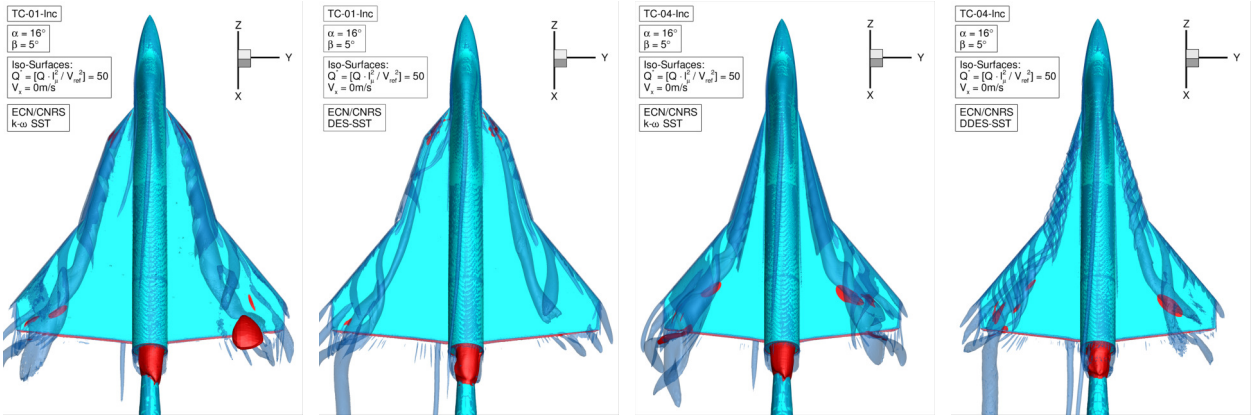

(a) NA1_W1 - k-ω SST **(b) NA1_W1 - DDES-SST** **(c) NA1_W2 - k-ω SST** **(d) NA1_W2 - DDES-SST**

Fig. 18 Vortical structures of the NA1_W1 and NA1_W2 configurations for α = 16° and β = 5°.

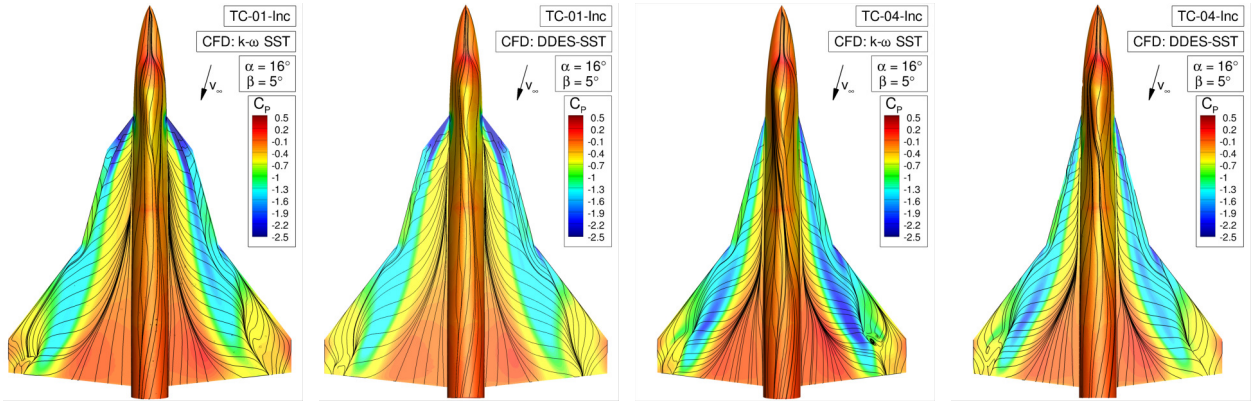

(a) NA1_W1 - k-ω SST **(b) NA1_W1 - DDES-SST** **(c) NA1_W2 - k-ω SST** **(d) NA1_W2 - DDES-SST**

Fig. 19 Surface pressure distribution and skin friction lines on NA1_W1 and NA1_W2 configurations for α = 16° and β = 5°.

Figure 20 shows the crosswise dimensionless axial velocity component at $x/c_r = 0.592$ for an angle of attack of 16°. For the NA1_W1 wing (see Figs. 20a, 20c and 20e), the TUM experiments reveal a strong asymmetry concerning the nature of the vortices developing on each wing. On the leeward wing, both IBV and MBV are jet-type vortices with a strong overshoot of axial velocity in the core of both vortices. On the windward wing, the IBV vortex is of wake type with a core axial velocity component close to zero at this section while the MBV vortex keeps its jet-type characteristic. Concerning the simulations, none of the turbulence closures is able to reproduce the right behaviour in the core of the IBV vortex on the leeward wing, $k-\omega$ SST providing a somewhat higher velocity than DDES-SST, but in both cases smaller than the measurements at this cross-section. Both simulations show two vortices very close to each other with opposite axial velocity distribution, while the TUM experiments show only one jet-type IBV vortex. On the windward wing, DDES-SST is the only model able to capture the strong decrease of the core axial velocity in the IBV vortex, k-ω SST yielding too strong axial velocities. Moreover, DDES-SST computations of the MBV vortex is in better agreement than what is obtained with k-ω SST.

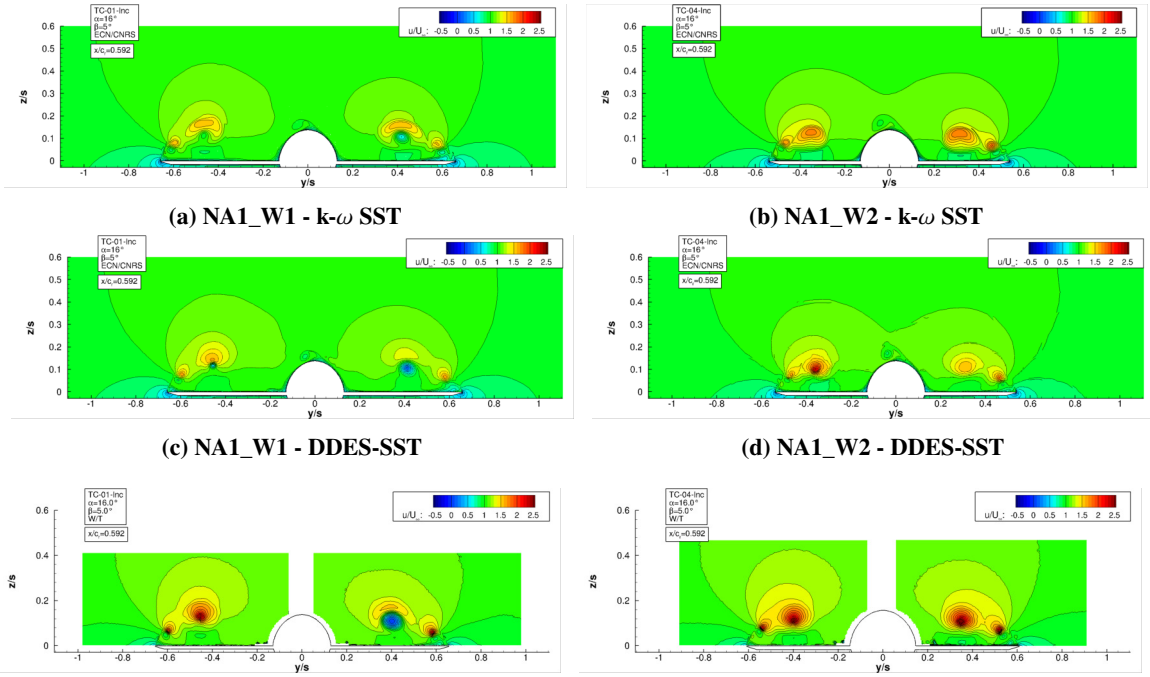

(a) NA1_W1 - k-ω SST **(b) NA1_W2 - k-ω SST**

(c) NA1_W1 - DDES-SST **(d) NA1_W2 - DDES-SST**

(e) NA1_W1 - TUM experiments **(f) NA1_W2 - TUM experiments**

Fig. 20 Axial component of the velocity at $x/c_r = 0.592$ for the NA1_W1 and NA1_W2 configurations at $\alpha = 16°$ and $\beta = 5°$.

For the NA1_W2 (see Figs. 20b, 20d and 20f), contrary to the previous wing configuration, the TUM experiments reveal more symmetric vortices developing on each wing. On the leeward and windward wings, both IBV and MBV are jet-type vortices with similar overshoots of axial velocity in the core of both vortices on leeward and windward sides. It is therefore interesting to see which turbulence closure is able to capture this different trend compared to NA1_W1, which will have a strong impact on the roll moment. Unfortunately, once again, there is no obvious winner. Although DDES-SST clearly captures the right overshoot in both IBV and MBV vortices on the leeward wing, it fails to reproduce the symmetric behaviour on the windward wing by predicting too weak an IBV vortex with an overshoot of 1.5 instead of the experimental of 2.5. On the other hand, the solution proposed by k-ω SST is more symmetric but, on both leeward and windward wings, the overshoots in the IBV and MBV vortex core are underestimated by a factor 2 (1.2 instead of 2.5).

Figure 21 (resp. 22) shows the dimensionless axial velocity, u/U_∞, in the inboard vortex (IBV) and mid-board vortex (MBV) cores for the angle of attack $\alpha = 16°$, on the leeward (resp. windward) wings. For NA1_W1, the leeward wing is characterised by an intense jet-type IBV vortex with a plateau of high velocity (around 2) from its onset and up to the trailing edge. $k-\omega$ SST predicts a plateau evolution but with a significantly lower core axial velocity around 1.0 while

the core velocity predicted by DDES-SST, decreases gradually from an initial accurate value of 2.0 at the onset to a lower value of 0.5 all along the second half of its trajectory. On the windward wing, TUM experiments show a rapid decay of the IBV core velocity which is very well predicted by DDES-SST while k-ω SST does not simulate this decay. For NA1_W2, he same high core velocity plateau is observed on the leeward wing, but now DDES-SST is able to capture it and provides a result clearly better than k-ω SST. On the windward wing, TUM experiments reveal the same high velocity plateau behaviour with a overshoot of from 2 to 2.5 during the main part of the progression while neither k-ω SST not DDES-SST are able to maintain this high velocity plateau, although DDES-SST captures a higher core velocity close to the onset.

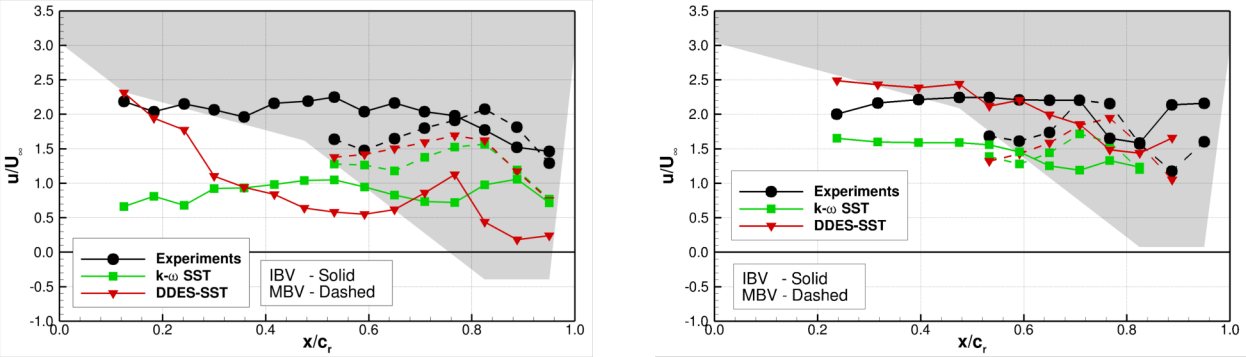

(a) Model NA1_W1 **(b) Model NA1_W2**

Fig. 21 Leeward wing - Dimensionless axial velocity for the IBV and MBV of the NA1_W1 and NA1_W2 configurations for α = 16°.

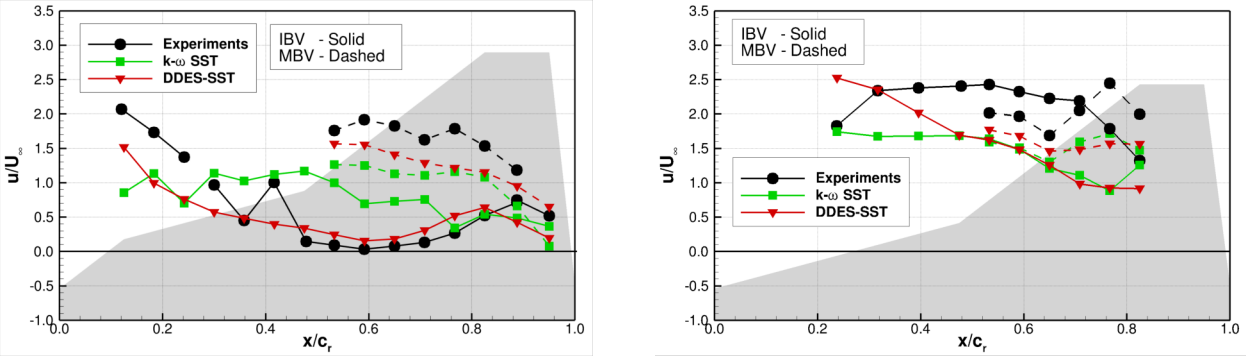

(a) Model NA1_W1 **(b) Model NA1_W2**

Fig. 22 Windward wing - Dimensionless axial velocity for the IBV and MBV of the NA1_W1 and NA1_W2 configurations for α = 16°.

3. Angle of attack α=24°

Figs. 23 and 24 show the vortical structures, surface pressure distributions and skin friction lines for NA1_W1 and NA1_W2 at 24°. For NA1_W1, DDES-SST predicts more intense vortical structures on both leeward and windward wings but the surface pressure and skin friction lines remain globally unchanged by the turbulence closures. For this angle of attack, a flow reversal is observed in the IBV vortex all along its trajectory on the windward wing while flow reversal occurs only close to the trailing edge of the leeward wing for both turbulence closures.

Figure 25 shows the crosswise dimensionless axial velocity component at x/c_r = 0.592 for an angle of attack of 24°. For the NA1_W1 wing (see Figs. 25a, 25c and 25d), the TUM experiments reveal a stronger asymmetry than what was observed previously at 16° concerning the nature of the vortices developing on each wing. On the leeward wing, both IBV and MBV vortices are clearly jet-type vortices with a strong overshoot of axial velocity in the core of both

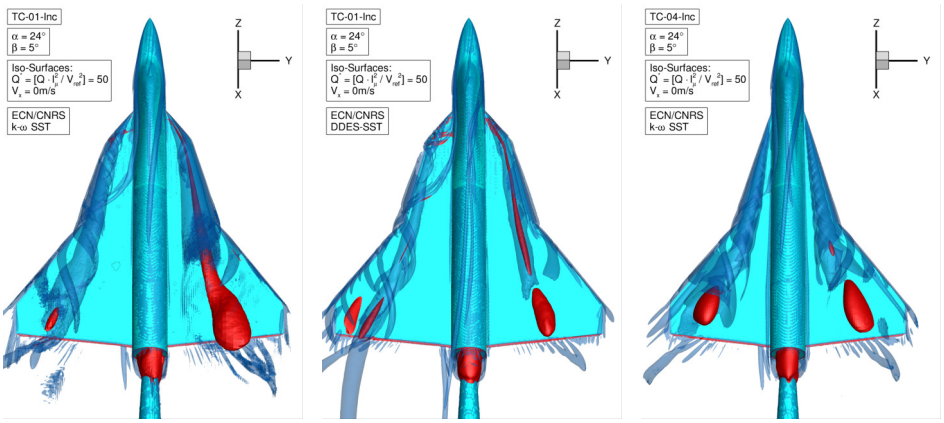

(a) NA1_W1 - k-ω SST **(b) NA1_W1 - DDES-SST** **(c) NA1_W2 - k-ω SST**

Fig. 23 Vortical structures of the NA1_W1 and NA1_W2 configurations for α = 24° and β = 5°.

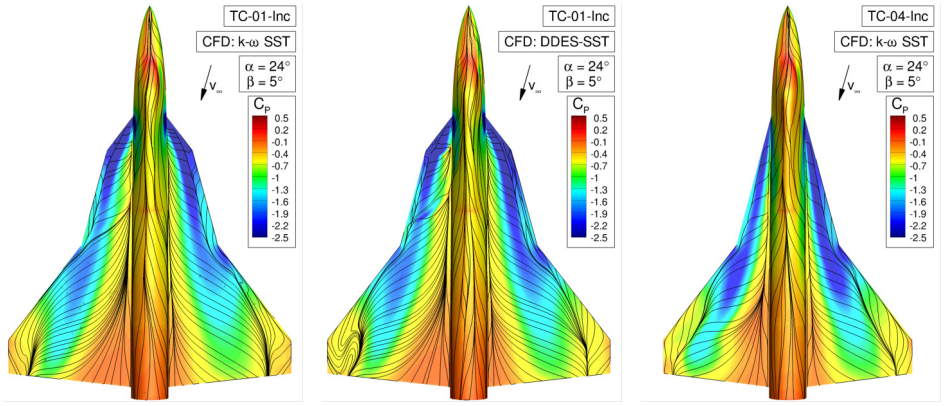

(a) NA1_W1 - k-ω SST **(b) NA1_W1 - DDES-SST** **(c) NA1_W2 - k-ω SST**

Fig. 24 Surface pressure distribution and skin friction lines on NA1_W1 and NA1_W2 configurations for α = 24° and β = 5°.

vortices (around 2.5 for IBV and 1.5 for MBV). On the windward wing as for 16°, the IBV vortex is of wake type with a core axial velocity component close to zero at this section while the MBV vortex keeps its jet-type characteristic. Concerning the simulations at this higher angle of attack, none of the turbulence closures is able to reproduce the right behaviour in the core of the IBV vortex on the leeward wing, $k-\omega$ SST providing a very similar velocity as DDES-SST, in both cases smaller than the measurements at this cross-section. As observed for the lower angle of attack, one can notice the existence of two zones very close to each other corresponding to two co-rotating vortices, the upper one with a velocity overshoot and the lower one with a velocity undershoot. Such a complex vortex-vortex interaction is not confirmed by TUM measurements at this location which show a unique jet-type vortex. On the windward wing, both k-ω SST and DDES-SST models are able to capture the strong decrease of the core axial velocity in the IBV vortex. Moreover, both models slightly overpredict the core velocity in the MBV vortex.

For the NA1_W2 (see Figs. 25b and 25e), contrary to what is observed at 16°, the TUM experiments reveal now a strongly asymmetric situation characterised by a very intense jet-type (resp. wake-type) vortices on the leeward (resp. windward) wing, the MBV vortex keeping however its jet-type configuration. $k-\omega$ SST simulations seem to capture the right trend described in the measurements, but the overshoot in the leeward IBV vortex is strongly under-estimated (1.5 instead of 3.0) and the negative axial component present in the core of the windward IBV vortex at this location is not reproduced by $k-\omega$ SST which predicts a value around 0.1 instead of -0.2. Moreover, the IBV vortex is surrounded by a region of high axial velocity in the k-ω simulation, which is visible in the experiments.

Figure 26 (resp. 27) shows the dimensionless axial velocity, u/U_∞, in the inboard vortex (IBV) and mid-board

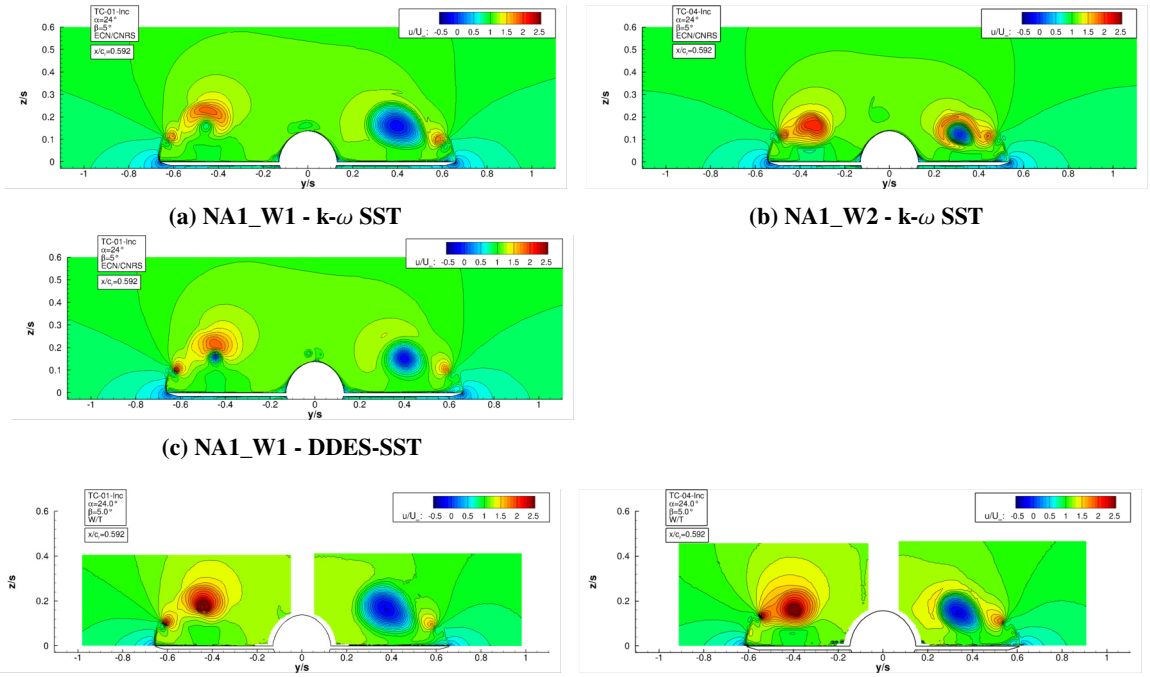

(a) NA1_W1 - k-ω SST **(b) NA1_W2 - k-ω SST**

(c) NA1_W1 - DDES-SST

(d) NA1_W1 - TUM experiments **(e) NA1_W2 - TUM experiments**

Fig. 25 Axial component of the velocity at x/c_r = 0.592 for the NA1_W1 and NA1_W2 configurations at α = 24° and β = 5°.

vortex (MBV) cores for the angle of attack α = 24°, on the leeward (resp. windward) wings. For NA1_W1, as noticed previously for an angle of attack of 16°, neither $k\omega$ SST nor DDES-SST are able to maintain the high core velocity plateau shown by the experiments with an overshoot of varying from about 2.5 to 2.0 during the IBV progression. k-ω SST predicts a too low core axial velocity all along the vortex trajectory and DDES-SST provides an even lower core axial velocity close to zero from the middle of the wing. On the windward plane, the flow reversal occurring in the core of the IBV vortex shown by the measurements is very accurately captured by DDES-SST while $k-\omega$ SST predicts too high a core axial velocity. The MBV core velocity is reasonably well predicted by both turbulence closures.
For NA1_W2, on the leeward wing, k-ω SST predicts a jet-type IBV vortex but the axial core velocity is underestimated (around 2.3 instead of 3.0) but the trend along the wing is reasonably well captured with a similar high axial velocity plateau which is maintained up to x/c_r = 0.6. On the windward wing, k-ω SST underestimates the core axial velocity close to the onset (2.6 instead of 3.2). Then, it appears to produce reasonably good results since the vortex breakdown is nicely reproduced for x/c_r around 0.4 and 0.6, and then followed by a region of zero core velocity up to the trailing edge.

4. DDES-SST - Analysis of the behaviour of the roll moment for α between 16° and 24° for NA1_W1

In Fig. 16b, we have noticed the irregular evolution of the roll moment between 16°and 24°. The roll moment computed by DDES-SST is negative like in the experiments at 16°. But at 20°, the roll moment keeps decreasing without being able to stay on the experimental plateau characterised by measured values of C_{mx} close to zero. This decrease of C_{mx} continues at 24° with an even more negative roll moment coefficient in complete contradiction with the plateau observed in the measurements. To try to relate this wrong roll moment evolution to the local flow characteristics, it is interesting to analyze the local flow behaviour specifically for these three angles of attack and compare with the solution provided by k-ω SST at 18° (less negative and therefore closer to the measurements) to understand what is missing at 20° and 24°.
Fig. 28 shows the axial velocity component at the usual cross-section x/c_r = 0.592 for all the above-mentioned angles of attack. All the angles of attack are computed with DDES-SST except 18° which is computed with k-ω SST. The velocity defect in the core of the IBV vortex on the windward wing increases with the incidence, which is the expected behaviour. But, for the leeward wing, one observes a non-monotonous evolution of the core axial velocity in the IBV vortex. The

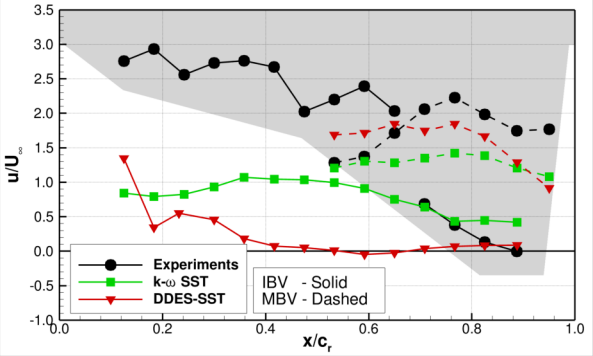

(a) Model NA1_W1

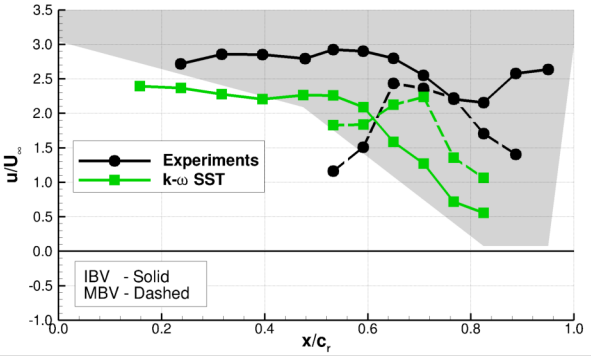

(b) Model NA1_W2

Fig. 26 Leeward wing - Dimensionless axial velocity for the IBV and MBV of the NA1_W1 and NA1_W2 configurations for α = 24° and β = 5°.

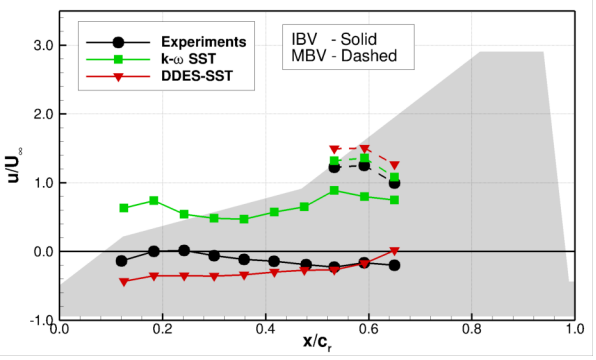

(a) Model NA1_W1

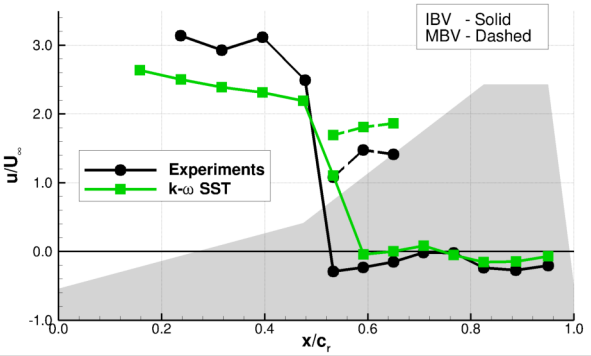

(b) Model NA1_W2

Fig. 27 Windward wing - Dimensionless axial velocity for the IBV and MBV of the NA1_W1 and NA1_W2 configurations for α = 24° and β = 5°.

axial velocity grows from 16° to 18° and then decreases at 20° to a value very similar to the one observed at 16°and continued its decay at 24°. The evolution observed at this cross-section $x/c_r = 0.592$ is actually confirmed all along the main part of IBV trajectory on the leeward wing upwind of this specific cross-section up to a specific cross-section which depends on the incidence. It is also worthwhile to mention that, on the leeward wing, the simulations do not exhibit a single IBV vortex but, instead, two vortices close to each other characterised by different core flow characteristics, a wake-type vortex close to the wall and a jet-type vortex on top of it. This two-vortices structure is maintained for these four different angles of attack, although less marked at 18° obtained with k-ω SST. This is in contradiction with the unique clear and coherent IBV vortex depicted in the measurements on the leeward wing.

In order to understand the origin of these two vortices observed the computed IBV vortex on the leeward wing, Figure 29 shows the evolution of the vortical structures from 16° to 24° over the whole plane. Already at 16° but more marked at 20° and 24° , one can see in the first quarter of the leeward wing the onset of one or several vortices (according to the incidence) parallel to the fuselage which are diverted towards the IBV vortex and interact with it according to various modalities. The interaction becomes more complex and occurs further downstream when the angle of attack increases. One can notice several local zones of flow reversal (in red) close to the location of this interaction. We believe that, downstream of this vortex-vortex interaction, the nature of the leeward IBV vortex changes from a jet-type (upwind of it) to a wake-type core (downwind of it). Interestingly, this interaction does not occur at 18° where k-ω SST is able to predict an almost zero roll moment in agreement with TUM measurements while for the incidences for which this interaction occurs, the roll moment keeps its negative value when computed with DDES-SST or k-ω SST. This local flow behaviour might be coincidental with no link of causality with the change of slope of the roll moment, but it would be valuable to pay more attention to this early vortex-vortex interaction, to assess if it is strongly dependent

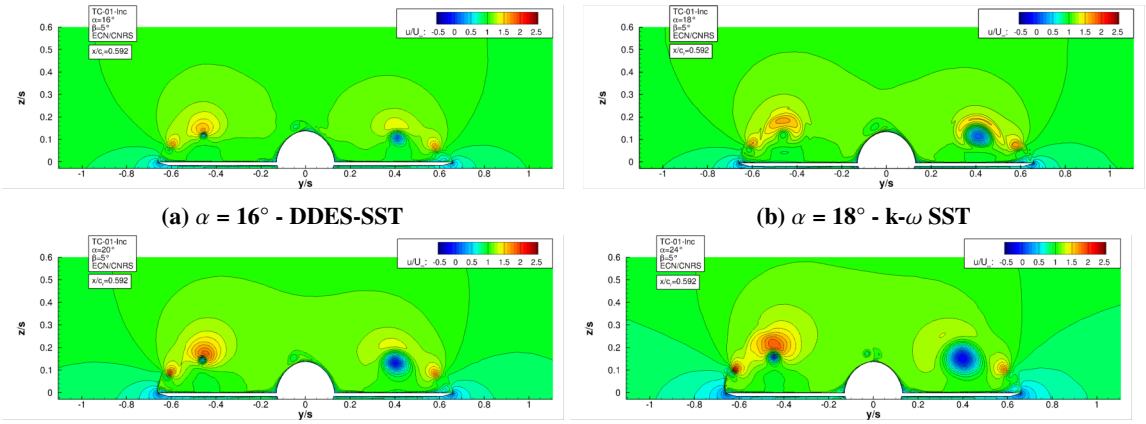

(a) α = 16° - DDES-SST **(b) α = 18° - k-ω SST**

(c) α = 20° - DDES-SST **(d) α = 24° - DDES-SST**

Fig. 28 NA1_W1 - Axial component of the velocity at x/c_r = 0.592 between α = 16° and α = 24°for β = 5°.

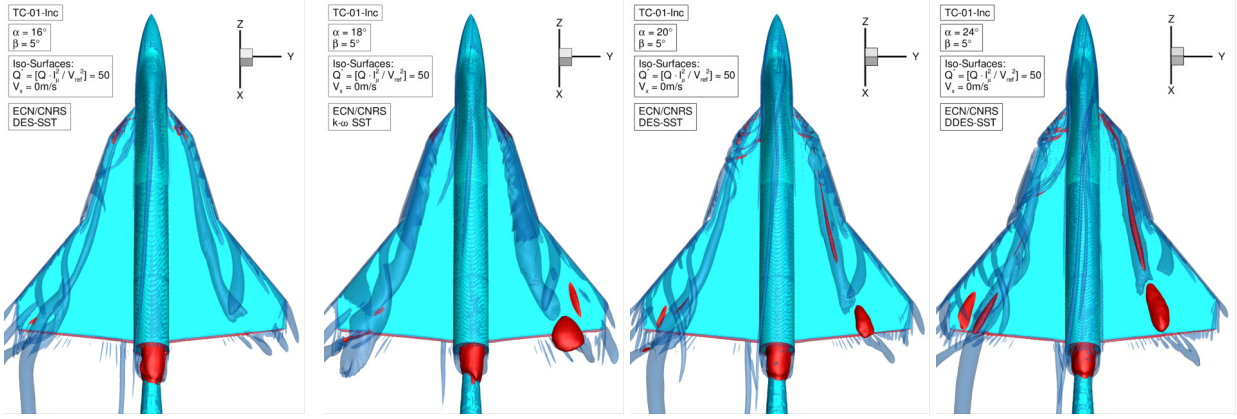

(a) α = 16° - DDES-SST **(b) α = 18° - k-ω SST** **(c) α = 20° - DDES-SST** **(d) α = 24° - DDES-SST**

Fig. 29 NA1_W1 - Vortical structures between α = 16° and α = 24°for β = 5°.

on the turbulence closure and confirmed or not by the measurements.

VI. Conclusions

This article was devoted to a global and local study of the flow around two different wing configurations, the so-called NA1_W1 and NA1_W2 geometries, for several angles of attack and two drift conditions. Two statistic k-ω SST and hybrid RANS/LES DDES-SST turbulence models were used on flow-adapted grids which capture automatically and efficiently the prominent vortical structures during their evolution. Systematic comparisons with TUM measurements were conducted on the forces and moments but also on the local flow details. Systematic vortex core analysis were provided, which can be used to assess the ability of CFD to represent the various jet-type or wake-type vortex behaviour all along the path of the main vortical structures present for each flow configuration. For the symmetric condition, the simulation performed with the help of DDES-SST, is globally equivalent to the one performed with k-ω SST for low angles of attack although DDES-SST is the only model able to capture accurately the vortex breakdown. For high angles of attack, the hybrid RANS/LES clearly shows its superior reliability. We have also noticed that the configuration NA1_W2 appears easier to simulate than NA1_W1 where vortex interaction occurs at lower angles of attack. The side-slip condition appears more complex to simulate for both wing configurations. Particularly, the lateral roll moment

change of sign occurring at a critical angle of attack is not satisfactorily modelled by the present computational approach, whatever the turbulence model used. These computations have at least established that this weakness is not related to a lack of local grid density but rather due to a modelling error affecting the vortical flow on the leeward wing. This is disappointing because the reliable prediction of the roll moment crisis is a key feature to assess the plane stability during maneuvers. By analyzing the local flow on the leeward wing for several incidences located close to the change of slope of C_{mx}, we propose that this modelling error is due to the early interaction between the computed fuselage vortices and the IBV vortex, not far from its onset. Based on TUM experiments, we suppose that this interaction does not occur in the same way in the real flow. This interaction strongly affects the core flow velocity longitudinal evolution and therefore impacts the very sensitive roll moment coefficient. This hypothesis will be assessed more rigorously in future studies.

Acknowledgments

The computations were performed using HPC resources from GENCI (Grand Equipement National de Calcul Intensif) (Grant-A0082A00129, Grant-A0102A00129) which is gratefully acknowledged.

References

[1] Jian, L., Kunyu, L., Haisheng, S., Yong, H., Zhitao, L., and Zhixiang, X., "Dynamic response of vortex breakdown flows to a pitching double-delta wing," *Aerospace Science and Technology*, Vol. 72, 2018, pp. 564–577.

[2] Boelens, O. J., Badcock, K. J., Elmilgui, A., Abdol-Hamid, K. S., and Massey, S. J., "Comparison of Measured and Block Structured Results for the F-16XL Aircraft," *Journal of Aircraft*, Vol. 46, No. 2, 2009, pp. 377–384.

[3] Hitzel, S. M., Winkler, A., and Hövelmann, A., "Vortex Flow Aerodynamic Challenges in the Design Space for Future Fighter Aircraft," *Notes on Numerical Fluid Mechanics and Multidisciplinary Design*, New results in Numerical and Experimental Fluid Mechanics XII. DGLR 2018., Vol. 142, edited by A. Dillman, G. Heller, E. Krämer, C. Wagner, C. Tropea, and S. Jakirlic, Springer, 2020, pp. 297–306.

[4] Pfnür, S., and Breitsamter, C., "Leading-Edge Vortex Interactions at a Generic Multiple Swept-Wing Aircraft," *Journal of Aircraft*, Vol. 56, No. 6, 2019, pp. 2093–2107.

[5] Queutey, P., and Visonneau, M., "An interface capturing method for free-surface hydrodynamic flows," *Computers & Fluids*, Vol. 36, No. 9, 2007, pp. 1481–1510.

[6] Leroyer, A., and Visonneau, M., "Numerical methods for RANSE simulations of a self-propelled fish-like body," *Journal of Fluids and Structures*, Vol. 20, No. 7, 2005, pp. 975–991.

[7] Deng, G. B., and Visonneau, M., "Comparison of explicit algebraic stress models and second-order turbulence closures for steady flows around ships," *In 7th International Conference on Numerical Ship Hydrodynamics*, 1999.

[8] Duvigneau, R., and Visonneau, M., "On the Role Played by Turbulence Closures in Hull Shape Optimization at Model and Full Scale," *J. Mar. Sci. Technol.*, Vol. 8, 2003, pp. 11–25.

[9] Cécora, R.-D., Radespiel, R., Eisfeld, B., and Probst, A., "Differential Reynolds-Stress Modeling for Aeronautics," *AIAA Journal*, Vol. 53, No. 3, 2015, pp. 1–17. Published online: 10 September 2014, March 2015.

[10] Guilmineau, E., Deng, B., G, Leroyer, A., Queutey, P., Visonneau, M., and Wackers, J., "Assessment of Hybrid RANS-LES Formulations for Flow Simulation around the Ahmed Body," *Computers & Fluids*, Vol. 176, 2015, pp. 302–319.

[11] Visonneau, M., Guilmineau, E., and Rubino, G., "Local Flow around a Surface Combatant at Various Static Drift Conditions: The Role Played by Turbulence Closures," *33rd Symposium on Naval Hydrodynamics*, Osaka, Japan, 2020.

[12] Wackers, J., Deng, G. B., Guilmineau, E., Leroyer, A., Queutey, P., and Visonneau, M., "Combined refinement criteria for anisotropic grid refinement in free-surface flow simulation," *Computers & Fluids*, Vol. 92, 2014, pp. 209–222.

[13] Mozaffari, S., Guilmineau, E., Visonneau, M., and Wackers, J., "Average-based mesh adaptation for hybrid RANS/LES simulation of complex flows," *Computers & Fluids*, Vol. 232, 2022, p. 105202.

[14] George, P. L., Hecht, F., and Vallet, M. G., "Creation of internal points in Voronoi's type method. Control adaptation," *Advances in Engineering Software*, Vol. 13, No. 5/6, 1991, pp. 303–312.

[15] Alauzet, F., and Loseille, A., "High-order sonic boom modeling based on adaptive methods," *Journal of Computational Physics*, Vol. 229, No. 3, 2010, pp. 561–593.